MX precipitate behavior in an irradiated advanced Fe-9Cr steel: Helium sequestration and cavity swelling performance

T.M. Kelsy Green[a*], Tim Graening[b], Weicheng Zhong[b], Ying Yang[b], and Kevin G. Field[a]

[a]University of Michigan-Ann Arbor, currently at Antares Nuclear Industries
[b]Oak Ridge National Laboratory
[a]University of Michigan-Ann Arbor

*Corresponding Author: kelsy@antaresindustries.com

Graphical Abstract

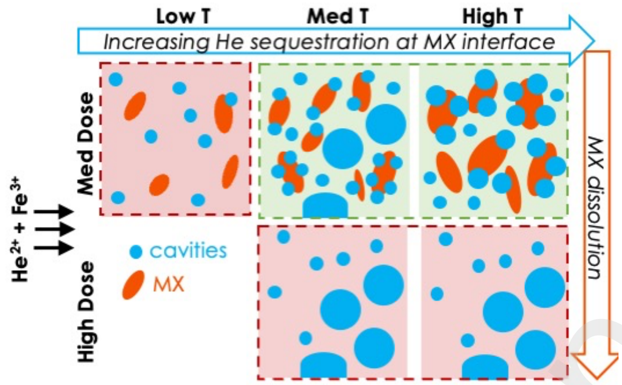

Abstract

This work is the third and final part in an initial series on addressing the behavior of MX precipitate stability in an advanced Fe-9Cr reduced activation ferritic/martensitic (RAFM) alloy under fusion-relevant ion irradiation conditions. Here, the helium trapping properties of MX precipitates are investigated across varying damage levels (15-100 dpa), temperatures (400-600°C), and helium doses (10-25 appm He/dpa) using sophisticated dual ion beam experiments and electron microscopy. Results indicate that MX precipitates efficiently sequester helium in the form of nanoscale bubbles at the precipitate-matrix interfaces near the peak swelling temperature (~5 bubbles/precipitate at 500°C). Swelling was primarily due to matrix cavities. The Fe-9Cr alloy reached 2% swelling by 100 dpa, suggesting a shift to steady-state swelling around 50 dpa at

500°C. However, MX precipitate dissolution beginning at 15 dpa did not coincide with this onset of steady-state swelling.

1.1 Introduction

Reduced activation ferritic/martensitic (RAFM) steels are able to achieve superior mechanical properties and reduced radioactivity during operation for fusion applications [1]. An important microstructural feature in RAFM steels is MX precipitates (M=metal, X=C/N), which is produced in the microstructure through compositional tailoring and thermomechanical treatment (TMT) as a means to improve high temperature mechanical properties [1,2]. MX precipitate-matrix interfaces may also serve the dual purpose of being trapping sites for point defects and transmutant products such as helium [2,3]. However, traditional RAFM steels under conventional processing methods, such as F82H or EUROFER97, lack a sufficient density of MX precipitates to meet the demands of high-temperature creep [4] and to provide the necessary swelling resistance by decreasing the steady-state swelling below ~0.2%/dpa in neutron irradiation environments [5].

To address this need, a new class of RAFM steels called Castable Nanostructured Alloys (CNAs) was developed with computational thermodynamics and traditional manufacturing methods to have an increased volume fraction of MX precipitates (~0.7 times less than the volume fraction of clusters in ODS steels but ~1.3-2.5 times greater than the MX phase fraction in traditional FM and RAFM steels) [6-11]. The performance and function of these MX precipitates under irradiation conditions is important to understand for continual alloy improvement and development for fusion applications, particularly for developing an understanding of the MX precipitates' dissolution behavior and helium sequestration ability as both of these may have significant effects on in-operation swelling.

The stability of MX precipitates in CNA steels has been the subject of recent work**.** Ref 12 and 13 addressed the stability of MX precipitation in an advanced Fe-9Cr CNA alloy called CNA9 under fusion-relevant ion irradiation conditions and concluded that the (i) precipitates had temperature-dominated responses at intermediate damage levels (≤15 dpa) under single beam irradiation, displaying observable ballistic dissolution effects at ≤400°C and radiation-enhanced coarsening ≥500°C; (ii) helium co-injection acted to suppress diffusion and hence suppress radiation-assisted coarsening of precipitates at high temperatures (500, 600°C) at 15 dpa but had no significant effect on precipitate dissolution for damage doses at and above 50; and (iii) precipitates dissolved between 15 and 50 dpa in all conditions tested regardless of temperature, dose, and the presence of implanted helium.

This work then addresses the MX precipitate population's ability to sequester helium before their dissolution. Efficient helium sequestration is needed to disperse helium homogenously throughout the matrix and prevent the helium-assisted growth of cavities. Though MX precipitates have been previously shown to sequester helium at their interfaces in Ti-modified austenitic stainless steel and delay the onset of steady-state swelling [14-16], literature lacks definitive evidence that this is also the case for MX precipitates in FM and RAFM steels like CNA9. Two previous generations of CNAs, CNA1 and CNA3, have been tested for helium and/or radiation damage effects at the time of this work [3, 17-19]. Parish *et al.* observed that 32% of all cavities in dual ion (Fe + He) irradiated CNA3 were connected to precipitate-matrix interfaces, though not all precipitates examined were MX precipitates [18]. Yan [3] and Lin *et al.* [19] also examined helium-filled bubble behavior in CNA1 and CNA3 with in-situ and ex-situ helium implantation to ~7,500 appm at 500 and 700°C and to 10,000 appm He at 500-900°C, respectively. Though the MX precipitates in the CNAs sequestered helium in the form of bubbles at their interfaces, the authors concluded the MX precipitates were not present in high enough densities to suppress matrix swelling. Importantly, studies conducted by Yan and Lin *et al.* only implanted helium and did not co-irradiate with other ions (such as Fe) that induced large amounts of lattice damage, thus not capturing the progression of precipitates and cavities with both helium implantation and significant ion damage.

This work assesses the capability and capacity of MX-TiC precipitate-matrix interfaces in CNA9 to sequester helium using high fidelity dual ion irradiations and conventional electron microscopy. Additionally, matrix swelling will be examined and evaluated in relation to MX precipitate stability. This work is the final part in a series assessing the co-evolution of precipitation and helium in the advanced 9Cr-RAFM steel alloy CNA9.

1.2 Methods

All methodology for sample procurement and processing, ion irradiation experiments, TEM sample preparation, and MX precipitate analysis are identical to and can be found in Refs. [12] and [13]. The experiments conducted for this work are shown in Table 1.

Regions of interest (ROIs) in the liftouts taken from irradiated bulk specimens were assessed with both scanning and conventional transmission electron microscopy (STEM, CTEM). First, ROIs were compositionally mapped with STEM-energy dispersive spectroscopy (STEM-EDS) to obtain size, density, and spatial location information on MX-TiC precipitation [13]. Next, Fresnel contrast in off-zone CTEM bright-field (BF) imaging was used to image cavities in the same ROIs, thus allowing for the location of cavities (in the matrix or on the precipitate-matrix interface) to be ascertained. Under- and over-focused images at ±1 μm (vendor indicated) were used to help identify cavities and underfocused images at -0.5 μm were used to estimate the size and density of the cavities. Cavities correlated with MX-TiC precipitates were identified by superimposing the CTEM BF images onto STEM-EDS maps of Ti. As the TEM-BF images are 2D projections of the 3D volume of the TEM lamellae, the distance between the cavity in the matrix and the precipitate may be 'flattened' and lead to an incorrect identification of the cavity as being attached to the precipitate. Though the precipitate-attached cavities were relatively identifiable as depicting a clear 'halo' around the circumference of the precipitates (*i.e.*, a higher localized density around a precipitate versus in the matrix), the possibility of mislabeling cavities in the matrix as being attached to precipitates cannot be fully accounted for. It is assumed that this error is small such as not to affect the overall results of the analysis. In addition, cavities that appeared "on top" of the precipitates by being within the projected precipitate radius were counted as being attached to the precipitate.

Spherical cavities less than 5 nm in diameter observed with CTEM are assumed to be helium-containing bubbles. The 5 nm cutoff was determined by the valley in the bimodal cavity size distribution at 500°C and was uniformly applied to all temperatures and conditions within. This is common practice in recent literature of similar studies [20-22], deriving from literature results that assume cavities populations with bimodal populations are helium filled at small sizes due to the theoretical derivations for cavity growth rates in the presence of helium for sub-critical and nanometer scaled cavities [23-27].

Table 1 Ex-situ dual beam irradiation parameters, showing the 'target parameter/achieved parameter' experimentally. T_{irr} = temperature of irradiation.

T_{irr} (°C)	Total dpa	Helium co-implantation rate (appm He/dpa)	Dose rate (dpa/s)
400/401.6	15/15.1	10/10.3	$7\times10^{-4}/7.1\times10^{-4}$
500/500.6	15/15	10/9.96	$7\times10^{-4}/7.3\times10^{-4}$
500/498	50/50	10/9.96	$7\times10^{-4}/7.3\times10^{-4}$
500/499.6	100/100	10/10.1	$7\times10^{-4}/7.3\times10^{-4}$
600/599.5	15/15.1	10/9.8	$7\times10^{-4}/7.1\times10^{-4}$

1.3 Results and Discussion

1.3.1 Temperature effects at intermediate damage level: 400, 500, and 600°C to 15 dpa with 10 appm He/dpa

This series of irradiations assesses the effects of temperature at 400, 500, and 600°C on cavity behavior to 15 dpa with 10 appm He/dpa. Ref. [13] found that precipitates at 400°C underwent partial dissolution, precipitates at 500°C were in a condition of stability, and MX precipitates at 600°C underwent significant radiation-enhanced growth (though helium co-injection suppressed this growth as compared to the single beam condition with no helium).

Cavity statistics for each condition are shown in Table 2. The size distributions of the cavities in the matrix (labeled 'Matrix') and attached to precipitates (labeled 'MX') is shown in Figure 1. The distribution of matrix cavities are also plotted on a log-log scale in Figure 2. Matrix cavities displayed a temperature-dependent behavior: a unimodal distribution of small, spherical cavities (~1-2 nm in diameter) was found in the 400°C (Figure 1a) and 600°C (Figure 1c) conditions, but a bimodal distribution of cavities was found in the 500°C condition (Figure 1b). The generally accepted mechanism that prevents cavity formation at low temperature is recombination and at high temperature is the thermal disassociation of cavities [23]. It is assumed that the bimodal cavity distribution at 500°C follows the generally accepted role of helium in cavity growth rates: hypo-critical pressurized cavities at small sizes (< 5 nm) and unconstrained growth for hyper-critical cavity sizes (>5 nm) [24-28]. In literature, a bimodal cavity size distribution signifies at or near peak swelling for a material whereas unimodal distributions correspond to values far-off peak swelling under common fission- and fusion-relevant irradiation conditions [28]. As seen in this study, the unimodal distributions at 400 and 600°C corresponded to off-peak swelling (≤0.005%) and the bimodal size distribution at 500°C to near-peak swelling (~0.2%)

(Figure 2). Thus, it is assumed within that 500°C is closest to the peak swelling temperature for the conditions tested. This is later confirmed based on the total swelling values observed at 100 dpa.

The general cavity behavior is shown in Figure 3 and representative STEM-EDS maps of Ti overlaid on the corresponding TEM-BF micrographs in the underfocused condition are shown for each condition assessed in Figure 4. The trapping ability of the MX precipitate-matrix interfaces was found to be temperature-dependent. The most efficient helium sequestration occurred at 500 and 600°C, with an average of number of 5.3±0.4 and 4.8±0.4 MX-TiC-attached bubbles per precipitate, respectively (Table 2). On the other hand, a statistically significant number of precipitate-attached bubbles was not found at 400°C.

The results at 400°C will be discussed first, centered on why bubbles did not form at the precipitate interfaces. The continual erosion of a clearly defined precipitate-matrix interface due to ballistic dissolution effects, which were dominant at this condition as noted in previous work [13], may have caused the decreased probability of helium bubble attachment to precipitates at low temperature. Such an erosion would change the local strain and misfitting dislocation structure, thus altering the local diffusion and capture of helium to the interfaces [13]. Additionally, the combination of low mobility for helium complexes through the matrix, enhanced point defect recombination at 400°C compared to elevated temperatures, and greater interparticle spacing from ballistic dissolution may have also retarded the nucleation rate of helium-filled bubbles in precipitate interfaces.

The following interconnected conclusions can be drawn on the helium-precipitate behavior near peak swelling temperature at 500°C: (1) the precipitate-attached cavities were all designated as bubbles and remained below the critical bubble radius of ~4 nm (Supplemental A); (2) unlike the matrix cavities, the precipitate-attached bubbles did not display a bimodal size distribution; and (3) virtually all swelling was derived from matrix cavities evidenced by the smaller sizes of the precipitate-attached bubbles versus the matrix cavities – the MX precipitates were not sites of enhanced vacancy collection [29]. This indicates that MX-TiC precipitates may effectively capture helium in FM and RAFM steels before undergoing dissolution at elevated damage levels (>15 dpa) during irradiation near the peak swelling temperature. To the authors knowledge, this is the first work to systematically observe helium sequestration capabilities for MX-TiC precipitates in the CNA class of materials under fusion-relevant ion irradiation conditions near peak swelling temperature.

Unlike the matrix cavities at 600°C, the precipitate-attached bubbles did not thermally disassociate with increasing temperature nor did they de-trap from the interface at 600°C. Rather, precipitate-attached bubbles grew in size, suggesting that helium had significant binding with the Ti and C in the MX precipitates or binding to the interface itself which prevented the thermal release of helium and vacancies into the matrix. This observation aligns with previous studies on CNA1 and CNA3, where MX precipitates effectively trapped helium at their interfaces at temperatures greater than 600°C under elevated temperature helium implantation [3, 19]. The binding of helium to the interfaces in combination with enhanced matrix diffusion of helium complexes may be responsible for the growth in precipitate-attached bubbles at 600°C as compared to 500°C. These results suggest the centrality of diffusion as the mechanism responsible for helium migration to precipitate-matrix interfaces traps.

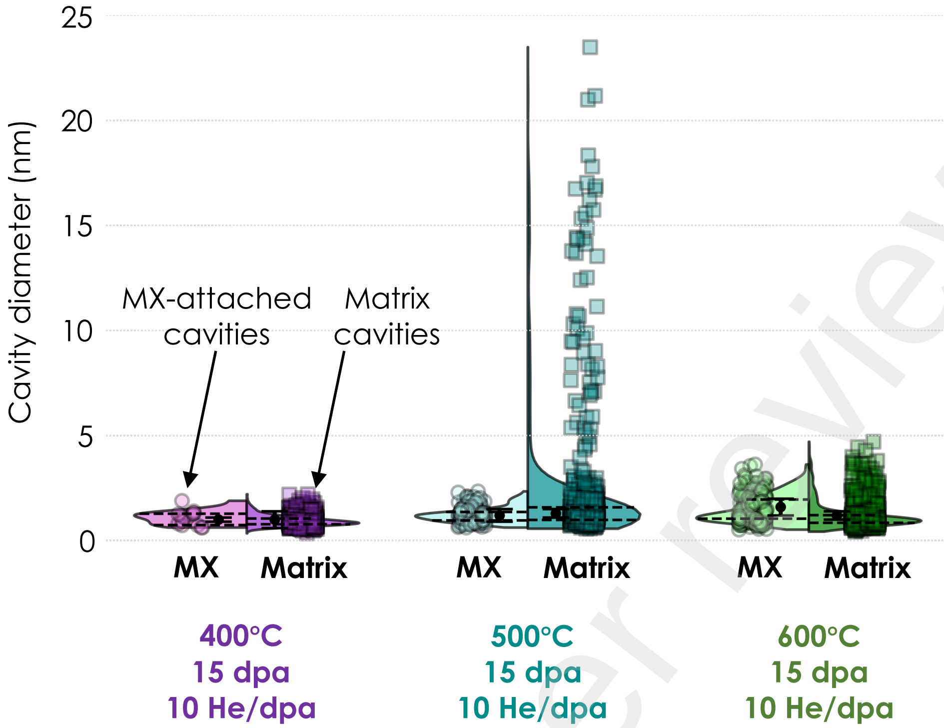

Figure 1 Comparison of precipitate-attached bubbles (circle symbols) to matrix cavities (square symbols) for the dual beam conditions at 400°C (purple), 500°C (blue) and 600°C (green).

181

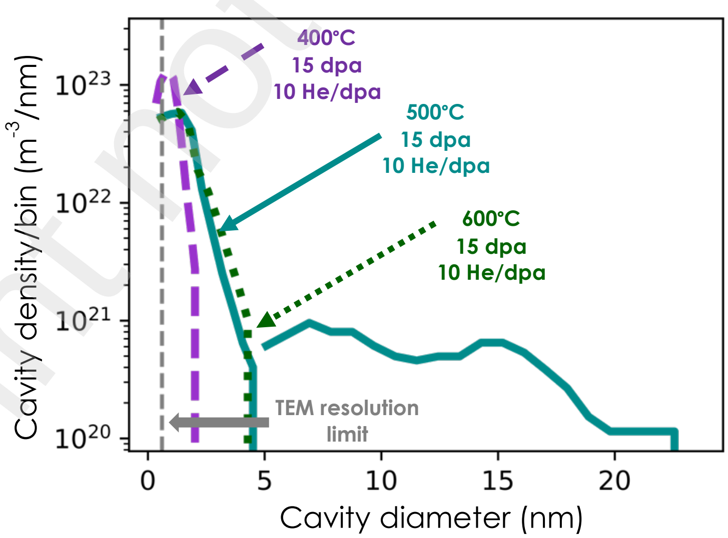

Figure 2 Cavity density versus cavity diameter for the conditions irradiated at 400 (dashed purple line), 500 (solid blue line), and 600°C (dotted green line), with 10 appm He/dpa to 15 dpa.

182

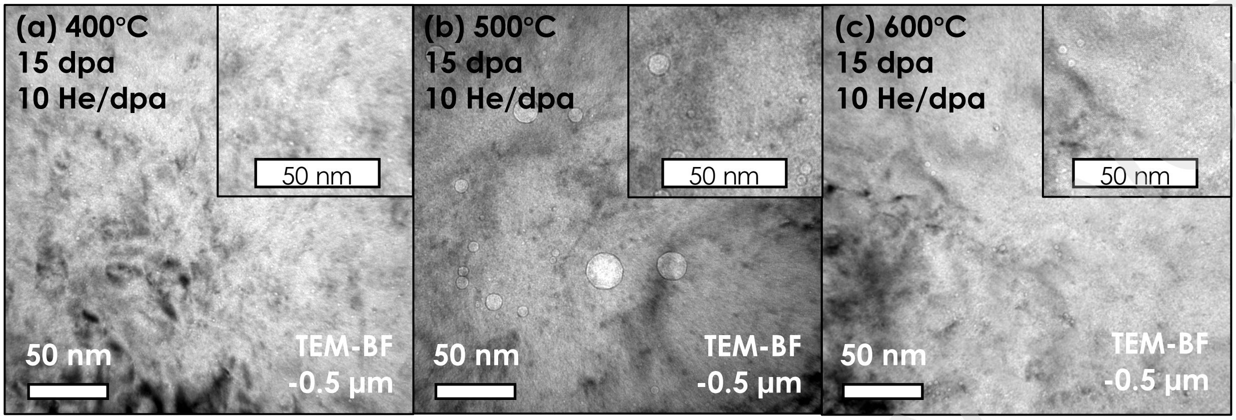

Figure 3 CTEM-BF underfocused images showing the general cavity behavior in the nominal damage region for the conditions irradiated to 15 dpa with 10 appm He/dpa series at (a) 400°C, (b) 500°C, and (c) 600°C.

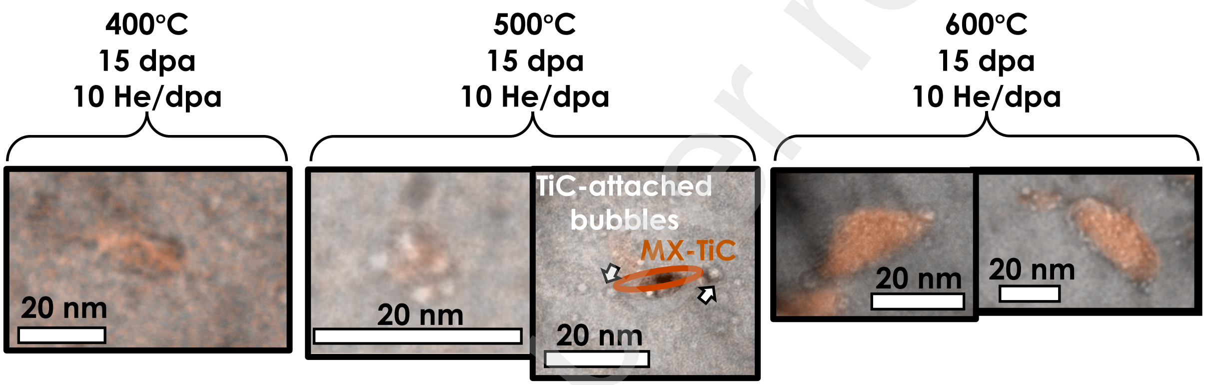

Figure 4 Representative STEM-EDS maps of Ti with corresponding TEM-BF micrographs in the underfocused condition overlaid for the 15 dpa 10 appm He/dpa series at 400, 500, and 600°C.

Table 2 Statistics of cavity analysis for dual beam irradiations at 400, 500, and 600°C to 15 dpa with 10 appm He/dpa and 7×10^{-4} dpa/s. N.O. means not observed.

Parameter	**400°C**	**500°C**	**600°C**
Number of total cavities studied	856 total	792 total	926 total
Number of TiC-attached cavities	14 (<5nm) 0 (>5nm)	162 (<5nm) 0 (>5nm)	366 (<5nm) 0 (>5nm)
Number of matrix cavities	842 (<5nm) N.O. (>5nm)	576 (<5nm) 54 (>5nm)	560 (<5nm) N.O. (>5nm)
Diameter of TiC-attached cavities	1.0±0.1 nm (<5nm) N.O. (>5nm)	1.2±0.03 nm (<5nm) N.O. (>5nm)	1.6±0.04 nm (<5nm) N.O. (>5nm)
Diameter of matrix cavities	1.0±0.04 nm (<5nm) N.O. (>5nm)	1.3±0.02 nm (<5nm) 10.1±0.4 nm (>5nm)	1.2±0.02 nm (<5nm) N.O. (>5nm)

Density of TiC-attached bubbles	$(0.06\pm0.02)\times10^{22}$ m^{-3} (<5nm)	$(0.5\pm0.05)\times10^{22}$ m^{-3} (<5nm)	$(0.8\pm0.07)\times10^{22}$ m^{-3} (<5nm) 0 (>5nm)
Density of matrix cavities	$(3.3\pm0.1)\times10^{22}$ m^{-3} (<5nm) N.O. (>5nm) (>5nm)	$(1.7\pm0.06)\times10^{22}$ m^{-3} (<5nm) $(0.1\pm0.01)\times10^{22}$ m^{-3} (>5nm)	$(1.3\pm0.08)\times10^{22}$ m^{-3} (<5nm) N.O. (>5nm) (>5nm)
Ratio of TiC-attached bubbles to the number of TiC precipitates observed	0.4±0.1	5.3±0.4	4.8±0.4
Fraction of precipitate-attached bubbles to total bubble count	0.02±0.006	0.3±0.03	0.5±0.04
Swelling from all cavities	0.002±0.0002%	0.2±0.01%	0.005±0.0002%

1.3.2 Helium co-implantation effects: 500°C to 15 dpa with 25 appm He/dpa

Ref. [13] found that there were no differences in MX precipitate behavior between the conditions irradiated at 500°C to 15 dpa with either 10 or 25 appm He/dpa. The general cavity behavior and the sequestration of helium at the precipitate-matrix interfaces of the condition with 25 appm He/dpa is shown in Figure 5. Comparing Table 2 to Table 3 shows that there is no statistically significant difference in the density or size of matrix or precipitate-attached cavities in the 25 appm He/dpa condition versus in the 10 appm He/dpa condition. Hence, the MX-TiC precipitates remain efficient helium sequestration sites at 25 appm He/dpa condition. As explained in Ref [13], a greater difference in helium rate is most likely needed to cause any significant differences in overall precipitate or cavity behavior.

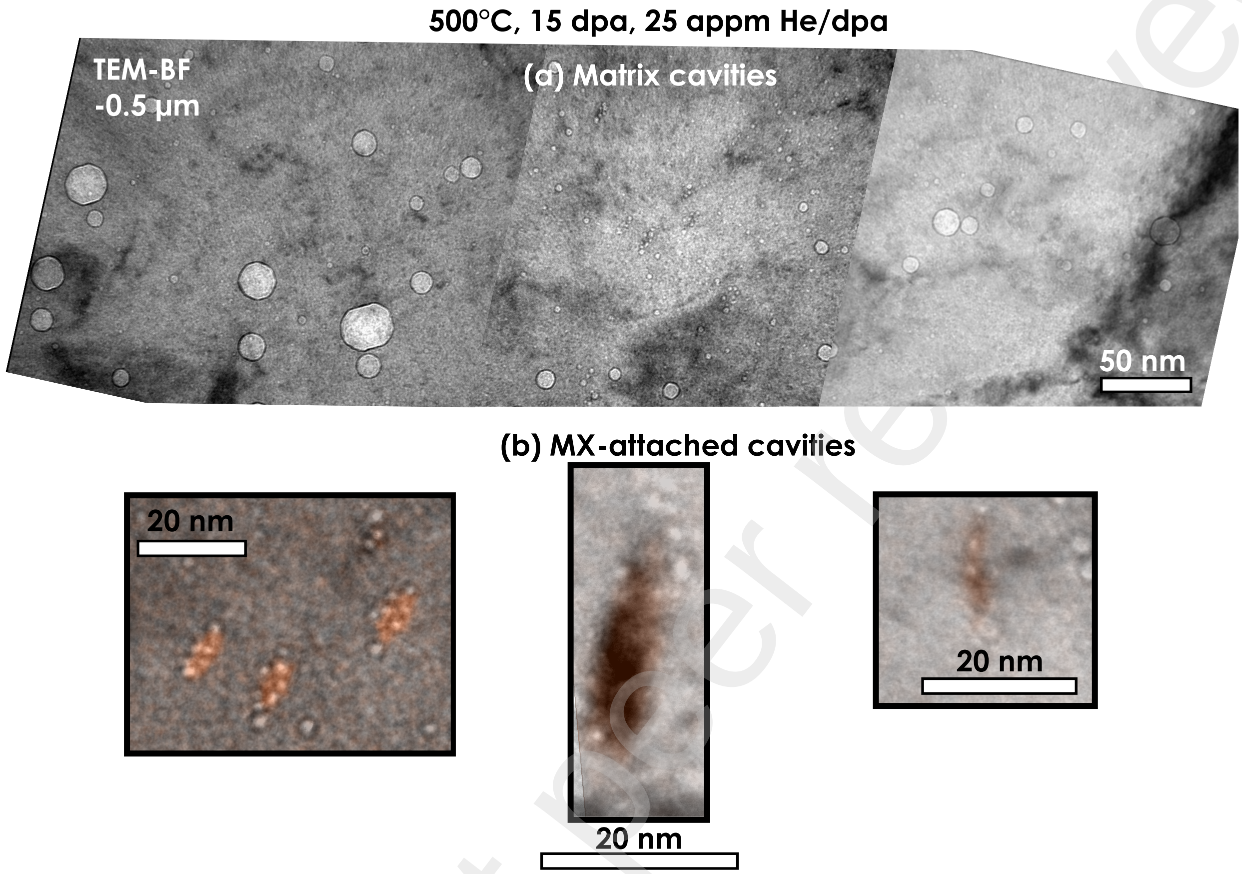

Figure 5 (a) TEM-BF underfocused images showing the general cavity behavior and (b) representative STEM-EDS maps of Ti with corresponding TEM-BF micrographs in the underfocused condition in the nominal damage region of the 500°C,15 dpa, 25 appm He/dpa condition.

Table 3 Statistics of cavity analysis for select dual beam irradiations at 500°C to 15 dpa with 25 appm He/dpa and 7×10-4 dpa/s.

Parameter	15 dpa 25 appm He/dpa
Number of total cavities	896 total
Number of TiC-attached cavities	173 (<5nm) 0 (>5nm)
Number of matrix cavities	670 (<5nm) 53 (>5nm)
Diameter of TiC-attached cavities	1.4±0.04 nm (<5nm) N.O. (>5nm)
Diameter of matrix cavities	1.5±0.01 nm (<5nm) 11.7±0.4 nm (>5nm)

Density of TiC-attached bubbles	$(0.7\pm0.1)\times10^{22}$ m^{-3} (<5nm)
Density of matrix cavities	$(3.1\pm0.1)\times10^{22}$ m^{-3} (<5nm) $(0.2\pm0.03)\times10^{22}$ m^{-3} (>5nm)
Ratio of TiC-attached bubbles to the number of TiC precipitates observed	5.6±0.0.3
Fraction of precipitate-attached bubbles to total bubble count	0.2±0.0.007
Swelling from all cavities	0.3±0.05%

1.3.3 Damage level effects at high damage levels: 500°C to 50 and 100 dpa with 10 appm He/dpa

Figure 6 shows representative TEM-BF micrographs of matrix cavities for the dual beam irradiations at 500°C to 15, 50, and 100 dpa with 10 appm He/dpa and 7×10^{-4} dpa/s. MX precipitates were dissolved by 50 dpa and remained dissolved at 100 dpa. Hence, no analysis of MX-attached cavities could be conducted in those conditions. The cavity statistics and swelling values are given in

Table 4. All conditions at 500°C exhibited bimodal cavity distributions (Figure 7). While the distributions of matrix bubbles remained largely unaltered between 15 and 100 dpa, there was an observable increase in the size of matrix voids as the damage level increased indicating continued growth with increasing dose.

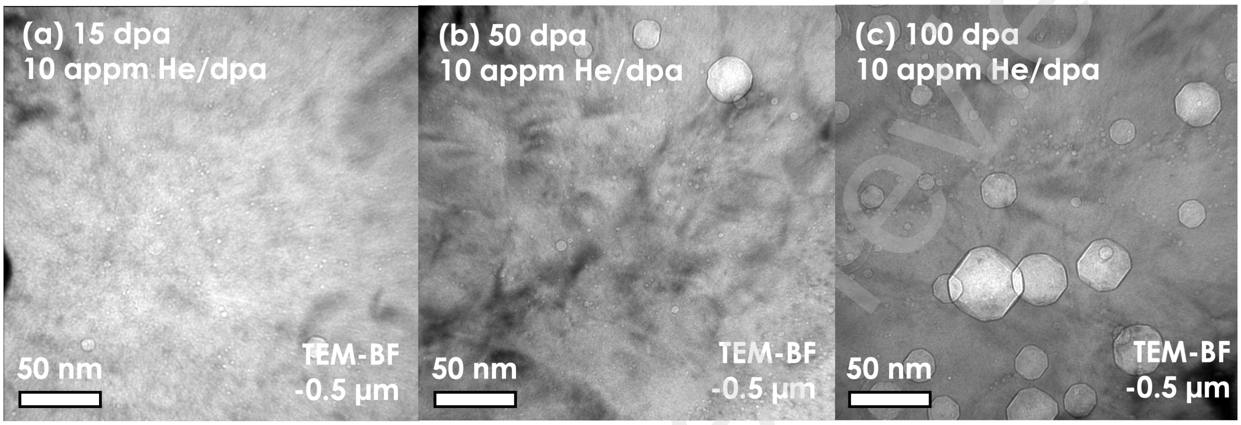

Figure 6 Cavity results for dual beam irradiations irradiated to (a) 15, (b) 50, and (c) 100 dpa. All conditions irradiated with 10 appm He/dpa at 500°C with a dose rate of 7×10^{-4} dpa/s. Images are TEM-BF micrographs in the -0.5 μm underfocused condition.

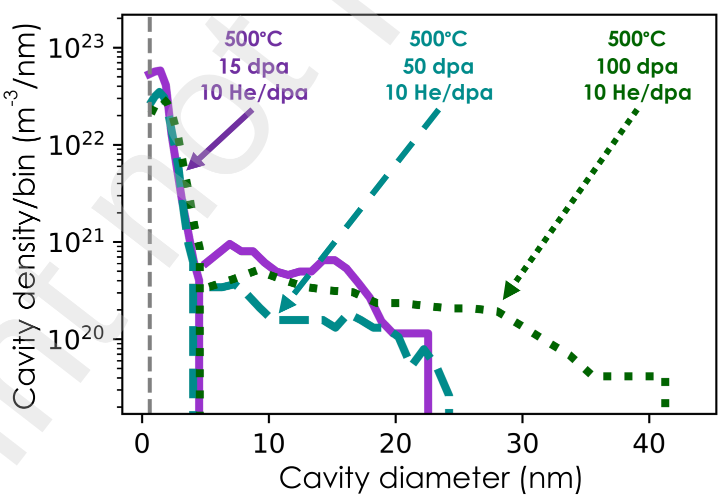

Figure 7 Cavity density versus cavity diameter for the conditions irradiated at 500°C with 10 appm He/dpa to 15 dpa (solid purple line), 50 dpa (dashed blue line), and 100 dpa (dotted green line).

Table 4 Statistics of cavity analysis for select dual beam irradiations at 500°C to 15, 50, and 100 dpa with 10 appm He/dpa and 7×10-4 dpa/s. The 15 dpa condition includes cavities in the matrix and attached to TiC precipitates. See Table 5.3 for a detailed analysis of cavities in the 15 dpa condition.

Parameter	15 dpa	50 dpa	100 dpa
Number of total cavities	792 total 738 (<5nm) 54 (>5nm)	568 total 539 (<5nm) 29 (>5nm)	619 total 548 (<5nm) 71 (>5nm)
Diameter of matrix cavities	1.3±0.01 nm (<5nm) 10.1±0.4 nm (>5nm)	1.6±0.07 nm (<5nm) 11.8±0.6 nm (>5nm)	1.9±0.02 nm (<5nm) 16.3±0.8 nm (>5nm)
Density of cavities	$(2.1\pm0.08)\times10^{22}$ m^{-3} total $(1.8\pm0.07)\times10^{22}$ m^{-3} (<5nm) $(0.1\pm0.01)\times10^{22}$ m^{-3} (>5nm)	$(2.5\pm0.2)\times10^{22}$ m^{-3} total $(2.3\pm0.2)\times10^{22}$ m^{-3} (<5nm) $(0.1\pm0.01)\times10^{22}$ m^{-3} (>5nm)	$(3.2\pm0.3)\times10^{22}$ m^{-3} total $(2.8\pm0.3)\times10^{22}$ m^{-3} (<5nm) $(0.4\pm0.02)\times10^{22}$ m^{-3} (>5nm)
Swelling from all cavities	0.2±0.01%	0.2±0.03%	1.9±0.4%
Swelling/dpa	0.01±0.0007 %/dpa	0.004±0.0006 %/dpa	0.02±0.004 %/dpa

1.3.4 Swelling behavior near peak swelling temperature

Figure 8 compares the swelling data for all 500°C irradiation conditions for CNA9 to swelling data from literature for FeCr steel alloys between temperatures 400-510°C [17, 18, 21, 30-36]. Numerical data used in Figure 8 are tabulated in Supplemental B Table S1. Generally accepted trends in swelling can be observed in Figure 8, namely that engineering alloys have better swelling resistance than model alloys and dual and triple ion beam irradiations caused greater swelling at the same dose and temperature than single ion beam irradiations. Based on the limited swelling data of CNA9, CNA9 exhibits comparable swelling behavior to other depicted FeCr steels. CNA9 had a swelling value of ~0.2% at both 15 and 50 dpa and a swelling value of ~2% at 100 dpa. From 50 to 100 dpa, CNA9 displayed a swelling rate of 0.03%/dpa. Therefore, CNA9 likely remained in the incubation and transient regimes from 15 to 50 dpa and approached steady-state swelling near 50 dpa.

Of particular interest is determining whether the MX precipitates had any impact on the swelling values of CNA9. The MX precipitates dissolved at some point between 15 and 50 dpa. However, CNA9 had the same swelling value at both 15 and 50 dpa, calling into question if the MX precipitates had any effect on the higher dose swelling behavior. In order to effect swelling, precipitates must be efficient and abundant traps for helium and/or vacancies. This work has showed that the precipitate-matrix interfaces efficiently trap ~5 helium-filled bubbles near peak swelling temperature, but the precipitation may not be abundant enough to divert a substantial amount of helium and vacancies to prevent in-matrix clustering and eventual cavity nucleation and cavity growth. Evidence for this may be that MX precipitates represent approximately only 5% of the total sink strength of CNA9 at 15 dpa (see appendices in Refs. [12] and [13]). Thus, precipitate dissolution may have negligible effects on the cavity evolution in the matrix when observed as an overall macroscopic property such as for steady state swelling responses. Recent unpublished work by Polselli *et al*. suggest that the precipitates dissolved by ~25 dpa [37].

The importance of a high density of precipitates, and thus a high sink strength derived from precipitates, has been investigated by various researchers. Xiu *et al.* studied the relationship between sink strength and swelling in three alloys of dual ion irradiated HT9, concluding that as the sink strength of an HT9 alloy increased the onset of steady-state swelling was delayed and the steady-state swelling rate was lowered [35]. The three datasets (ACO3-HT9, FCRD-HT9, and ASB-HT9) are shown in Figure 8. Work on previous CNA generations by Yan *et al.* concurred that a high sink strength of precipitates (~10^{16} m^{-2}) was necessary to suppress bubble growth [19]. Zinkle *et al.* likewise determined that particle density of 10^{24} m^{-3} (in ODS steels) is needed to suppress deleterious changes in engineering properties under irradiation [2,36].

Based on literature and the current experimental results, the dissolution of the low-sink strength MX precipitates (~10^{13} m^{-2}) by 50 dpa is theorized to have a negligible impact on the high dose (>50 dpa) swelling behavior of CNA9. However, this assessment is based on a limited dataset of only three data points for CNA9 and at accelerated ion irradiation dose rates, emphasizing the need for a more detailed examination of damage levels and dose rate for a comprehensive analysis.

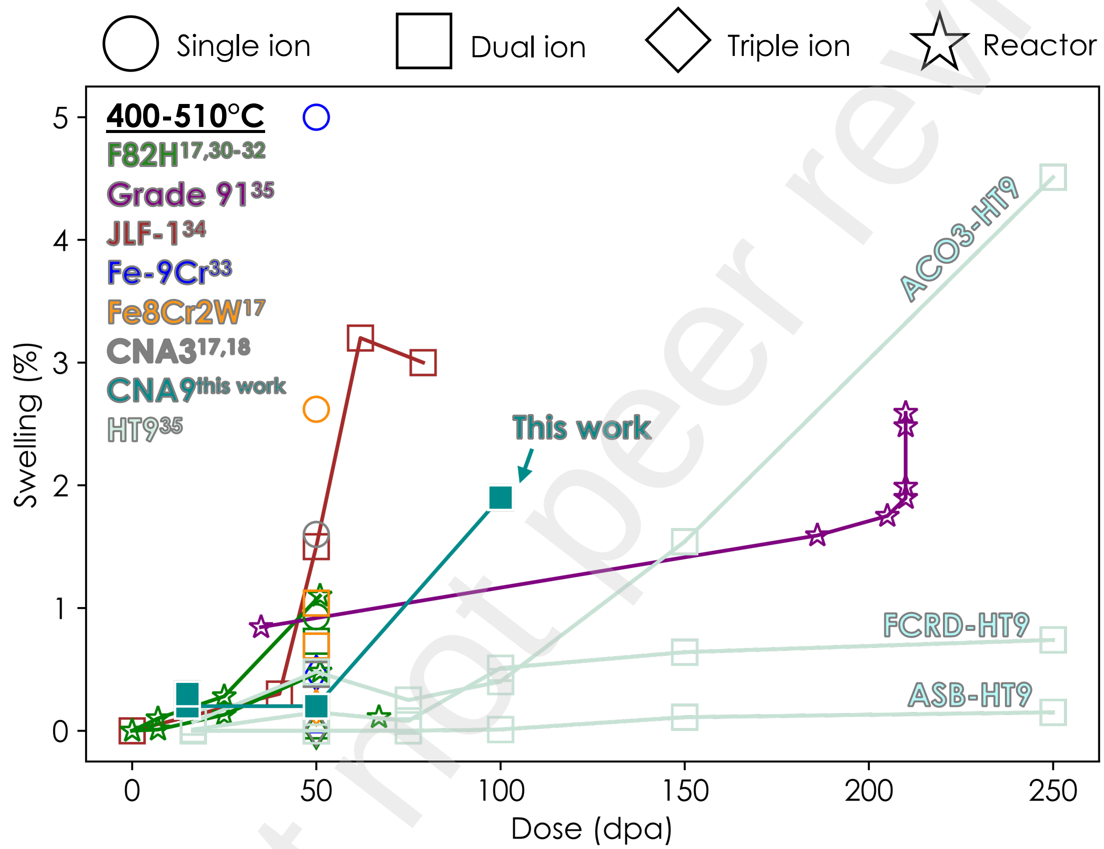

Figure 8 Comparison of swelling as a function of damage level (dpa) between CNA9 and RA/FM steels. See Table S.1 in the Supplemental section for tabulated values. Adapted from Ref. [36].

1.4 Conclusion

The matrix cavity behavior and the MX precipitate-attached bubble behavior in an advanced Fe-9Cr RAFM alloy called CNA9 was assessed under fusion-relevant ion irradiation conditions, leading to the following conclusions:

- MX precipitate-matrix interfaces efficiently sequestered helium-filled bubbles during irradiations with co-injected helium at 500 and 600°C when the precipitates remained stable or coarsened. Importantly, the MX precipitates contained an average of ~5 helium-filled bubbles per MX precipitate near the peak swelling temperature (500°C).
- Elevated temperature (500, 600°C) was needed to allow for sufficient diffusion of helium to precipitate-matrix interfaces to induce cavity formation and growth at said interfaces.
- The precipitate-attached bubbles did not thermally disassociate at 600°C unlike the matrix bubbles, showing the MX-TiC precipitates have a high binding energy with helium.
- CNA9 displayed similar swelling to other FeCr FM and RAFM alloys at the conditions assessed, though additional data points are needed for a full swelling assessment.
- However, the relatively low density of pre-existing MX precipitates (~10^{21} m^{-3}) is hypothesized to not affect helium-driven swelling in the matrix at elevated doses.
- The precipitates also dissolved sometime between 15-50 dpa and hence could not provide any sites for helium trapping at high damage levels, where swelling becomes increasingly detrimental. This is also tied to Ref. [13] of this research series, where it was hypothesized that the MX precipitates may have dissolved due to their low volume fraction. Hence, a greater number density of precipitates may benefit swelling resistance and possibly phase stability in RAFM alloys.
- Future FM and RAFM alloys for fusion applications need to increase the number density of precipitates to suppress swelling and ensure their stability to high damage levels (>100 dpa), but also must ensure the precipitates have a high binding energy for helium as the MX-TiC precipitates were shown to have.

This work systematically showed the helium sequestration capabilities of MX precipitates in an advanced RAFM steel under fusion-relevant ion irradiation conditions near peak swelling temperature. In conclusion, this research in combination with Ref [SI] and Ref [DI] has laid a the groundwork for understanding the fundamental behavior of MX precipitates in FM and RAFM steels under dual ion irradiation conditions, including the mechanisms of their stability and their ability to sequester helium and prevent swelling.

Acknowledgements

The experimental work presented here was funded by the Fusion Energy Sciences program (DOE-FOA-0002173). The authors also acknowledge the University of Michigan-Ann Arbor College of Engineering for financial support and the Michigan Center for Materials Characterization for use of the instruments and staff assistance. Research presented here was also partially supported by the Laboratory Directed Research and Development program of Los Alamos National Laboratory under project number XXPV. This research was partly sponsored by US Department of Energy, Office of Fusion Energy Sciences under contract DE-AC05-00OR22725 with UT-Battelle, LLC.

References

1. H. Tanigawa, E.G., T. Hirose, M. Ando, S.J. Zinkle, R. Lindau, E. Diegele, Development of benchmark reduced activation ferritic/martensitic steels for fusion energy applications. Nuclear Fusion, 2017. 57(092004).
2. Zinkle, S.J., et al., Multimodal options for materials research to advance the basis for fusion energy in the ITER era. Nuclear Fusion, 2013. 53(10).
3. Yan, Z. and Y. Lin, The effect of sink strength on helium bubble formation at elevated temperatures. Nuclear Analysis, 2022. 1(1).
4. Green, T.M.K., et al., Effect of N2- and CO2-containing shielding gases on composition modification and carbonitride precipitation in wire arc additive manufactured grade 91 steel. Additive Manufacturing, 2022. 56.

5. Aitkaliyeva, A., et al., Irradiation effects in Generation IV nuclear reactor materials, in Structural Materials for Generation IV Nuclear Reactors. 2017. p. 253-283.
6. Tan, L., Y. Katoh, and L.L. Snead, Development of castable nanostructured alloys as a new generation RAFM steels. Journal of Nuclear Materials, 2018. 511: p. 598-604.
7. Tan, L., Development of Nanoprecipitates- Strengthened Advanced Ferritic Alloys for Nuclear Reactor Applications. 2019.
8. Tan, L., L.L. Snead, and Y. Katoh, Development of new generation reduced activation ferritic-martensitic steels for advanced fusion reactors. Journal of Nuclear Materials, 2016. 478: p. 42-49.
9. Tan, L., et al., Recent status and improvement of reduced-activation ferritic-martensitic steels for high-temperature service. Journal of Nuclear Materials, 2016. 479: p. 515-523.
10. Tan, L., et al., Stability of MX-type strengthening nanoprecipitates in ferritic steels under thermal aging, stress and ion irradiation. Acta Materialia, 2014. 71: p. 11-19.
11. Tan, L., Y. Katoh, and L.L. Snead, Stability of the strengthening nanoprecipitates in reduced activation ferritic steels under Fe2+ ion irradiation. Journal of Nuclear Materials, 2014. 445(1-3): p. 104-110.
12. T. M. Kelsy Green and Tim Graening and Weicheng Zhong and Ying Yang and Kevin G. Field, "MX precipitate behavior in an irradiated advanced Fe-9Cr steel: Self-ion irradiation effects on phase stability," arXiv:2407.10002 [cond-mat.mtrl-sci], 13 July 2024, https://doi.org/10.48550/arXiv.2407.10002.
13. T. M. Kelsy Green and Tim Graening and Weicheng Zhong and Ying Yang and Kevin G. Field, "MX precipitate behavior in an irradiated advanced Fe-9Cr steel: Helium effects on phase stability," arXiv:2407.19589 [cond-mat.mtrl-sci], 22 July 2024, https://doi.org/10.48550/arXiv.2407.19589.
14. L.K. Mansur, W.A.C., Mechanisms of helium interaction with radiation effects in metals and alloys: A review. Journal of Nuclear Materials, 1983. 119: p. 1-25.
15. Kesternich, W., Helium trapping at dislocations, precipitates and grain boundaries, in Radiation Effects. 1983. p. 261-273.
16. Maziasz, P.J., Helium trapping at Ti-rich MC particles in Ti-modified austenitic stainless steel, ORNL, Editor. 1980.
17. Clowers, L.N., Z. Jiao, and G.S. Was, Synergies between H, He and radiation damage in dual and triple ion irradiation of candidate fusion blanket materials. Journal of Nuclear Materials, 2022. 565.
18. Parish, C.M., et al., Helium sequestration at nanoparticle-matrix interfaces in helium + heavy ion irradiated nanostructured ferritic alloys. Journal of Nuclear Materials, 2017. 483: p. 21-34.
19. Lin, Y.-R., et al., Bubble formation in helium-implanted nanostructured ferritic alloys at elevated temperatures. Acta Materialia, 2021. 217.
20. Taller, S., et al., Predicting structural material degradation in advanced nuclear reactors with ion irradiation. Sci Rep, 2021. 11(1): p. 2949.
21. Taller, S., The Role of Damage Rate on Cavity Nucleation with Co-Injected Helium in Dual Ion Irradiated T91 Steel, in Nuclear Engineering. 2020, University of Michigan.
22. Emelyanova, O., et al., Bubble-to-void transition promoted by oxide nanoparticles in ODS-EUROFER steel ion implanted to high He content. Journal of Nuclear Materials, 2021. 545.
23. Was, G.S., Fundamentals of Radiation Materials Science: Metals and Alloys. 2nd ed. 2017: Springer.

24. W.A. Coghlan, L.K.M., Critical radius and critical number of gas atoms for cavities containing a van der waals gas. Journal of Nuclear Materials, 1984. 122 & 123: p. 495-501.
25. A. Hishinuma, L.K.M., Critical radius for bias-driven swelling - A further analysis and its application to bimodal cavity size distributions. Journal of Nuclear Materials, 1983. 118: p. 91-99.
26. Kohnert, A.A., M.A. Cusentino, and B.D. Wirth, Molecular statics calculations of the biases and point defect capture volumes of small cavities. Journal of Nuclear Materials, 2018. 499: p. 480-489.
27. R.E. Stoller, G.R.O., Analytical solutions for helium bubble and critical radius parameters using a hard sphere equation of state. Journal of Nuclear Materials, 1985. 131: p. 118-125.
28. Bhattacharya, A. and S.J. Zinkle, Cavity Swelling in Irradiated Materials, in Comprehensive Nuclear Materials. 2020. p. 406-455.
29. Mansur, L.K., Theoretical evaluation of a mechanism of precipitate-enhanced cavity swelling during irradiation. Philosophical Magazine A, 1981. 44(4): p. 867-877.
30. E. Wakai, N.H., Y. Miwa, J.P. Robertson, R.L. Klueh, K. Shiba, S. Jistukawa, Effect of helium production on swelling of F82H irradiated in HFIR. Journal of Nuclear Materials, 2000. 283-287: p. 799-805.
31. Wakai, E., et al., Swelling behavior of F82H steel irradiated by triple/dual ion beams. Journal of Nuclear Materials, 2003. 318: p. 267-273.
32. T. Morimura, A.K., H. Matsui, Void swelling of Japanese candidate martensitic steels under FFTF/MOTA irradiation. Journal of Nuclear Materials, 1996. 239: p. 118-125.
33. Tanaka, T., et al., Synergistic effect of helium and hydrogen for defect evolution under multi-ion irradiation of Fe–Cr ferritic alloys. Journal of Nuclear Materials, 2004. 329-333: p. 294-298.
34. H. Ogiwara, H.S., H. Tanigawa, M. Ando, Y. Katoh,A. Kohyama, Void swelling in reduced activation ferritic/martensitic steels under ion beam irradiation to high fluences. Journal of Nuclear Materials, 2002. 307-311: p. 299-303.
35. Xiu, P., Effects of Sink Strength and Irradiation Parameters on Defect Evolution in Additively Manufactured HT9, in Nuclear Engineering and Radiological Sciences). 2022, University of Michigan.
36. Zinkle, S.J., et al., Development of next generation tempered and ODS reduced activation ferritic/martensitic steels for fusion energy applications. Nuclear Fusion, 2017. 57(9).
37. Polselli, E., Personal Communication. 2024.